From May 2009 *High Frequency Electronics*

Compact Antennas with Reduced Mutual Coupling for Wireless Sensor Networks

By Constantine G. Kakoyiannis, Penelope Gika and Philip Constantinou
National Technical University of Athens

This article examines the sinusoidal printed meander line antenna in wireless sensor nodes, and presents a method of reducing mutual coupling with a defected ground structure

Printed sinusoidal monopoles are a type of meander line antennas, with smooth curve structure and enhanced performance, suitable for building compact multi-element antennas (MEAs). The antennas described here were designed at 2-3 GHz to meet the size and bandwidth constraints of multimedia sensor networks. Their performance was characterized in terms of electrical size, bandwidth, and broadband radiation efficiency. We also studied compact printed arrays built with sinusoidal monopoles; we designed a two-element MEA and tested its behavior for interelement spacing ranging from $0.25\,\lambda_0$ to $0.10\,\lambda_0$. Array response was characterized in terms of VSWR bandwidth, mutual coupling, and broadband envelope correlation. Results show that densely-packed compact arrays feature controllable element detuning, whereas envelope correlation stays below 0.5 even for $\lambda_0/10$ spacing. If coupling and correlation suppression is needed, we describe a simple yet effective technique that offers multi-decibel gains. It is based on disturbance of the ground currents by insertion of a defect.

Introduction

The last decade has witnessed a tremendous amount of interest in low bit rate wireless sensor networks (WSNs). Recently, the WSN discipline started to shift towards the delivery of multimedia content. The integration of low-power wireless networking technologies with inexpensive hardware such as CMOS cameras and microphones is now enabling the development of distributed, networked systems that transfer video and audio streams, still images, and scalar sensor data. This effort will result in distributed networked systems known as Wireless Multimedia Sensor Networks (WMSNs) [1]. Multimedia content requires data rates that exceed those of current sensor nodes by orders of magnitude. Hence, large bandwidth must be added to the *de facto* constraints of small node size and low cost manufacturing. The need for bandwidth becomes even more pronounced if we consider that source encoding requires complex encoders and powerful processing algorithms, which leads to high energy consumption [1].

Sensor devices are severely constrained in terms of battery, memory, processing capability, and achievable data rate. They communicate over short distances. The miniaturization of sensor nodes is evolving at five different technological fronts: Antennas, RF circuits, digital baseband circuits, battery chemistries, and sensory circuits. Antennas have been rather immune to miniaturization, because the physical laws that determine their behavior cause their basic attributes to be self-conflicting. Hence, the art of antenna miniaturization is an art of compromise: The early work by Wheeler, Chu, and Harrington was the first step to confirm mathematically the intuition we have that the product efficiency × bandwidth is related to the volume occupied by the antenna [2, 3].

Multimedia sensors will be battery-operated, with non-replaceable batteries. Therefore, energy consumption is a fundamental issue associated with network lifetime and connec-

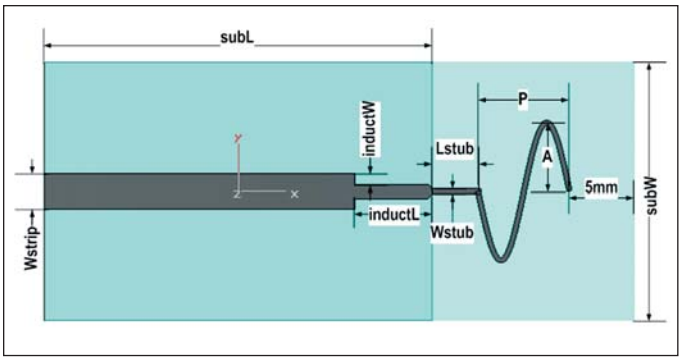

Figure 1 · A typical sinusoidal monopole. The element is built up by two half-periods of a sinusoid, and is thus termed "second iteration sinusoidal monopole" (*i* = 2). The substrate material is transparent so that the ground plane on the bottom layer is visible. Element size is 2*A* × 2*A* mm².

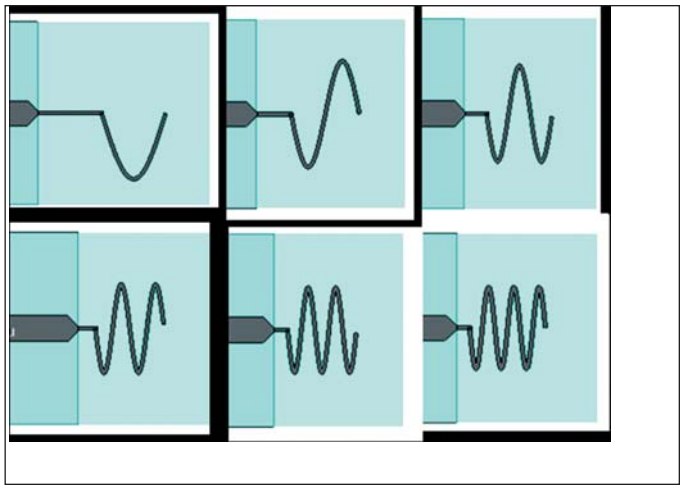

Figure 2 · Evolution of the sinusoidal antenna. From left to right, top row shows iterations *i* = 1, 2, 3; bottom row shows *i* = 4, 5, 6.

tivity. The efficiency of the radiating system is related to the energy efficiency of the whole node, decibel-for-decibel. Therefore, antennas designed for WSNs should exhibit efficiencies as close to unity as possible.

The theoretical foundations of small antennas suggest that good performance is obtained when most of the allocated space participates in the radiation mechanism [2, 3]. Thus, printed antennas, which are inherently 2-D structures, would seem to be handicapped. However, it was shown that printed meander-line antennas (MLAs) can operate as small efficient radiators for WSN nodes [4, 5].

Herein, a way to re-engineer the MLA is described [6]: By shaping the meander like a smooth sinusoidal curve, we obtained small antennas that can easily produce a second frequency-adjacent resonance, and thus greatly improve their operational VSWR bandwidth (BW_V). To the best of the authors' knowledge, the sinusoidal structure has been studied very few times in the past [7, 8]. The focus in these prior studies was on wire antennas that operated with large ground planes (GNDPs). Our work is the first attempt to integrate sinusoidal monopoles into portable devices. In [8] the authors showed that one of the properties of the sinusoidal antenna is that it is resonant despite its reduced height. Our study showed that sinusoids have a much more significant property: They can be easily designed to enter the unmatched and non-resonant region, where bandwidth is greatly enhanced.

After establishing a design guide for sinusoidal antennas and calculating their merits, we used this monopole as a building block to design compact arrays for sensor nodes [9]. We studied the effect of element proximity in terms of detuning and VSWR bandwidth, in the presence of strong mutual coupling. We calculated the envelope correlation as a function of interelement distance, to see how beneficial this structure is for diversity and MIMO systems. Mutual coupling degrades energy efficiency in transmit mode, and decreases the total received power in receive mode. In case of severe correlation, we suggest a simple, yet efficient, technique to reduce the coupling: We disturb the return currents on the GND plane with a non-periodic photonic bandgap (PBG) structure known as the defected ground structure (DGS). This work is a straightforward and cost-effective step towards the fabrication of directional and smart antennas for sensor networks.

Description of the Sinusoidal Antenna Scheme

A typical example of the antenna under study is shown in Figure 1. The antennas operate around 2.5 GHz. A two-layer PCB is made of low-cost FR4 material shown in blue (ε_r = 4.6, tanδ = 0.0170, H = 1.60 mm). The size of the PCB represents the whole size of the sensor node. On the top layer we etch the printed antenna and the microstrip line that excites it. On the bottom layer there is a continuous copper cladding that serves as the GNDP of both the antenna and the microstrip. The GNDP was removed below the antenna. It was assumed that all RF and baseband ICs and discrete components would be soldered on the bottom layer in an actual WSN node.

On the left side of this model we placed the SMA coaxial connector. To avoid the computational complexity, we replaced the round connector with an equivalent connector having square cross-section [10]. Since the copper trace of the antenna element is very narrow, we mitered the other end of the microstrip to reduce radiation at the width step. The antenna element comprises an initial straight segment and an integer number of half-periods of a sinusoidal curve. The number of half-periods, *i,* is the iteration of the antenna.

All significant dimensions that control the design of the antenna are depicted in Figure 1. In Figure 2 we show the evolution of the antenna up to the 6th iteration. The sinusoidal curve is characterized by its amplitude A and spatial period P. The initial straight segment is very crucial to the operation of the antenna: It drives the first horizontal segment away from the GNDP and improves the efficiency of the antenna. We set its length equal to a half-period ($L_{\text{stub}} = P/2$), which is adequate but by no means optimal; this is a subject of future work. The design is deterministic and thus totally repeatable. The copper segments that produce the sinusoidal curve are formed by (x, y) points obeying the parametric description of (1), where ξ is the independent parameter.

$$\left.\begin{aligned} x &= \xi \\ y &= -A\sin\left[2\pi\left(\frac{\xi}{P}-\frac{1}{2}\right)\right] \end{aligned}\right\} \qquad (1)$$

Our study indicated the input impedance $Z_{\text{in}}(j\omega)$ of the sinusoidal antenna is capacitive, as is typical of meander-line structures. To exploit this effect even further, we narrowed the last segment of the microstrip, which serves as an inductor in series with $Z_{\text{in}}(j\omega)$; it is the simplest matching network. The length of this "lumped element" is 18° at 2.5 GHz. The main point in the design guide of these antennas is that the series inductor can be combined with the width of the element W_{stub} to shape the input reflection coefficient in the frequency domain, and thus tailor the bandwidth to the designer's needs.

It is a trivial optimization task to show that minimum "antenna spread" on the PCB is achieved when the outline, or "envelope," of the element becomes square. Since sinusoids are folded monopoles, their unfolded length is constrained to be somewhat greater than $\lambda_0/4$. This constraint imposes an equivalent constraint on the sum of the two sides of the envelope, because of spatial uniformity. Turning the envelope into a square produces the envelope with the shortest diagonal, hence the smallest spread on the PCB. To enforce the square envelope, the dimensions of the sinusoidal antenna are constrained according to (2):

$$2A = \frac{P}{2}(i+1) \qquad (2)$$

Numerical Results and Radiation Properties

The antennas were designed and simulated in a reliable full-wave Transient Solver [11], which exhibited good correlation between simulated and measured results in our earlier studies [4], [5].

The numerical results in Figures 3 and 4 show some of the merits of sinusoidal antennas. Sinusoids are very wideband, covering the range 2.0-3.5 GHz. They clearly behave as dual-resonant antennas, since a second frequency-adjacent resonance is evident. The achievable bandwidths are much greater than what is needed for video transmission, e.g., in surveillance sensor networks. In such networks, MPEG-coded video traffic demands only a few MHz per channel. Such great bandwidths could even accommodate uncoded video transmissions. The designer is offered the choice to trade some of the available video bandwidth (BW_V) for further antenna miniaturization. In any case, the achievable VSWR bandwidth is about 68% greater than the one reached by the square meander-line monopole (S-MLM) of corresponding size and radiation efficiency that was studied in [5]:

$$\left.\begin{aligned} BW_{V,\,\text{Sinus}} &= 1.43\ \text{GHz} \\ BW_{V,\,\text{S-MLM}} &= 0.85\ \text{GHz} \end{aligned}\right\}$$

The BW_V is defined at VSWR = 1.92, i.e., for a return loss level $|S_{11}|^2$ –10 dB. The antennas were designed in such a way that the lower

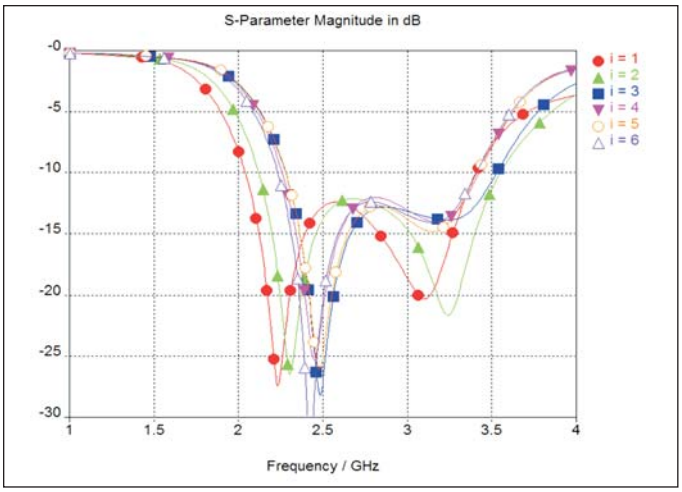

Figure 3 · Input reflection coefficient of the first six iterations of the sinusoidal antenna. The antenna exhibits a second resonance at an adjacent frequency, which shifts the center frequency of the band to 2.75 GHz.

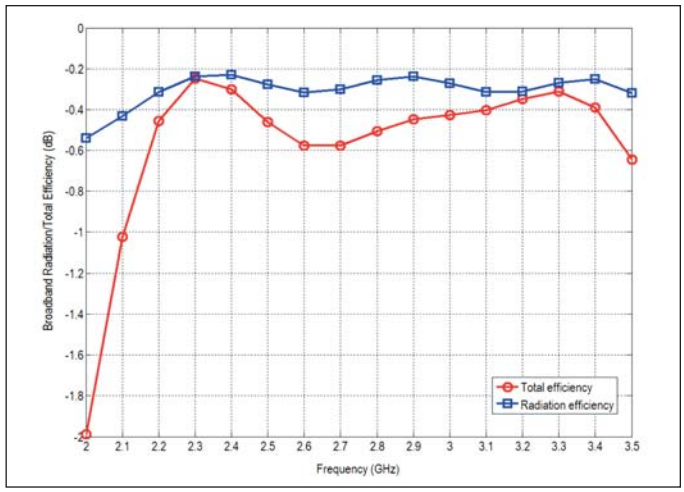

Figure 4 · Variation of total efficiency $e_{total} = e_{rad} \times (1 - |S_{11}|^2)$ in the 2.0-3.5 GHz range for the sinusoidal antenna with $i = 2$. In the band of interest the total loss in gain is less than 0.7 dB (e_{total} >85%).

resonance appears at or below 2.5 GHz. The upper resonance extends the usable band up to 3.5 GHz and shifts the center frequency upwards in the range $2.7 < f_c < 2.9$ GHz. Because of the dual-mode operation, the reflection coefficient at midband is $S_{11} = -12$ dB, i.e., the antennas are non-resonant at the "saddle point" where the two resonances join.

Moreover, the total efficiency is high throughout the band of interest; the loss in gain for the 2nd-iteration antenna is at most 0.7 dB in the band of interest. These results are valid for the nominal dimensions of the GNDP (see Table 2). We have studied the performance of the sinusoidal up to the 6th iteration. As is clearly seen in Table 1, the size of the element saturates at 8.6×8.6 mm at the last iteration. Thus, in terms of miniaturization, there is little sense in designing beyond the 5th iteration. All dimensions listed in Table 1 are compatible with standard PCB printing processes on FR-4 material, providing for straightforward and low-cost manufacturing.

Radiation Properties of the Single-Element Sinusoidal Antenna

In this section we comment on the radiation and polarization properties of printed sinusoidal antennas. We used as a typical example the 3rd-iteration monopole ($i = 3$), which displays its first resonance near 2.5 GHz. The numerical three-dimensional gain patterns shown in Figure 5 have been calculated at resonance, and indicate that the printed structure radiates like an asymmetrical dipole. It has a typical toroidal pattern, which shows stronger radiation towards the back side of the PCB, because of the presence of the ground plane. Actually, the radiation pattern corresponds to a thick asymmetric dipole. The achievable gain in estimated 0.5 dB higher than that of the half-wavelength dipole; a large part of the gain comes from the strong currents on the GND plane: The surface current distribution occupies a larger volume inside Wheeler's radiansphere compared to a thin printed straight dipole, hence the greater gain.

Another interesting point is that the omni-directional gain pattern shown in Figure 5 is very desirable for small portable terminals, such as wireless sensor nodes. These terminals often operate in a rich-scattering environment, where incoming waves arrive from all directions in space, i.e. they have a large angular spread [12]. In this case, terminals need to be able to receive efficiently from as many directions as possible. The 3D pattern shows that reception problems occur only along the x-axis.

Getting into the polarization details, the numerical results showed that the polarization at the principal planes is linear, but in general this antenna is elliptically polarized: The two orthogonal polarizations co-exist and

i	*A* (mm)	*inductW* (mm)	*Wstub* (mm)	*P* (mm)	*Lstub* (mm)
1	7.2	1.0	0.7	14.4	7.2
2	5.6	1.0	0.7	7.5	3.75
3	5.0	0.6	0.65	5.0	2.5
4	4.6	0.6	0.6	3.7	1.85
5	4.4	0.4	0.55	2.9	1.45
6	4.3	0.4	0.5	2.5	1.25

Table 1 · Dimensions for every sinusoidal scheme.

Wstrip (mm)	*inductL* (mm)	*subW* (mm)	*subL* (mm)
2.7	6.0	20.0	30.0

Table 2 · Parameter values common to all antennas.

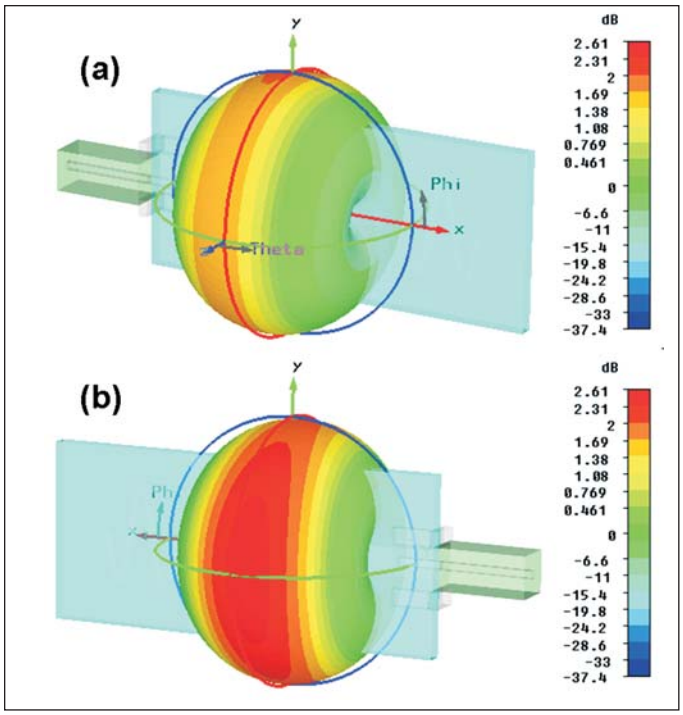

Figure 5 · The three-dimensional far-field pattern of the *i* = 3 antenna calculated at the resonant frequency of 2.5 GHz and embedded in the sensor node: (a) Front side of the PCB, $0 < \theta < \pi/2$, and (b) Back side of the PCB, $\pi/2 < \theta < \pi$. Radiation is stronger toward the back, due to the strong currents on the ground plane.

have similar magnitudes. Thus, the dominant E-field component changes at every principal plane:

- At $\varphi = 0$, the radiated wave is θ-polarized with a cross-polarization ratio (XPR) equal to XPR = 35 dB,
- At $\varphi = \pi/2$, the wave is φ-polarized with XPR = 28 dB,
- At $\theta = \pi/2$, the wave is φ-polarized with XPR = 35 dB.

The mixed polarization is a result of the 2-D surface current on the element and on the GNDP.

Notes on the Simulation Setup

The simulation guidelines described in this section apply to all microwave structures discussed in this work.

The antennas were designed and simulated by means of a Transient Solver [11], which is part of a full-wave electro-magnetic simulator that uses the Finite Integration Technique (FIT) to reformulate Maxwell's integral equations into the so-called Maxwell Grid Equations. In the time domain, by applying Yee's spatial discretization and time-stepping scheme, FIT results in the same set of equations as FDTD. The discretization of objects in space is done with a hexahedral mesh, as is typical with time-domain solvers. The possibility of a tetra-

hedral mesh also exists, but only when FIT is applied in the frequency domain.

The structures were excited by a wideband Gaussian Pulse (DC - 5 GHz), and the simulations were terminated when the initial excitation energy decayed by 50 dB. This was a good trade-off between simulation speed and truncation error in the FFT engine that translates the results from the time- to the frequency-domain. The maximum cell size at the maximum frequency f_{max} (smallest wavelength λ_{min}) was set at $\lambda_{min}/25$. The solvable space was terminated at several Berenger PML layers:

- During the initial design stages, four layers were used to speed up the design cycle, with distance-to-boundary equal to $\lambda/8$.
- For the final simulations, we used six layers, with distance-to-boundary equal to $\lambda/4$. An increase of the distance to $\lambda/2$ does not improve the results further.

Whenever a model featured topological symmetry and satisfied the appropriate boundary conditions for electric and magnetic flow, a magnetic wall was placed across the plane of symmetry, reducing the computational burden by one-half, because only half of the structure needed to be solved. The complexity of the models in terms of Yee cells ranged between 250,000 and 650,000 cells. Complexity depends upon the size of the GNDP and the level of detail exhibited by the antenna element.

Building Compact Multi-Element Antennas

Antennas for wireless sensors cannot be characterized, either through simulation or measurement, by being mounted on an infinite or large conducting ground plane. With miniature integrated antennas operating at 2-3 GHz, the ground plane dimensions will certainly be less than the operating wavelength and will closely approach the size of the antenna. In fact, this finite GND plane becomes an integral component of the radiator [5].

It is well understood from small antenna theory that, if the size of an antenna is decreased arbitrarily, all important attributes will suffer. The small antenna challenge can be interpreted as the right compromise between the three fundamental parameters: Gain, bandwidth, and size. However, for small radiators spread across a rich scattering environment, gain and radiation pattern seem to be irrelevant [12]. Radiation efficiency paints a more accurate picture of the antenna-under-test. To quantify the aforementioned trade-off, we used the ratio in (3) as a Figure-Of-Merit (FOM) for the antennas we designed. The goal of the designer is to come up with configurations that produce the largest possible ratio [4].

$$\mathrm{FOM} = \frac{10 \times \overline{e_{total}} \times FBW_V}{ka} \qquad (3)$$

i	subW (mm)	subL (mm)
3	18	26

Table 3 · The optimum ground plane dimensions, which resulted from the GNDP study of the third-iteration antenna.

i	BW_V (GHz)	f_{center} (GHz)	*FBWv* (%)	*ka* (rad)	e_{rad}	e_{total}	*FOM* (dB)
3	1.248	2.906	42.9	1.23	0.92	0.83	4.6

Table 4 · Overall performance results from the ground plane study of the third-iteration antenna (6).

In (3), FBW_V is the fractional VSWR bandwidth. The product ka is the electrical size of the radiator; k is the wavenumber and a is the radiansphere according to Wheeler [2]. The radiansphere is defined in Figure 6. The sphere is large enough to include the GNDP along with the element, since strong radiating currents flow across the GNDP surface. These currents can be seen in the surface current distribution shown in Figure 6. The quantity that is related to radiation is the total radiation efficiency averaged over the band of interest, e_{total}. The FOM is a pure number, and we express it in decibels. For further details on the definition of the FOM and the rationale behind the use of e_{total}, the reader is referred to [4].

Taking the above into consideration, we focused on the third-iteration sinusoidal antenna (i = 3), and performed a secondary study [6] to obtain suitable dimensions for the ground plane. According to this, the antenna optimizes the trade-off between its fundamental attributes when the GNDP becomes 26 × 18 mm in size ($0.22\,\lambda_0 \times 0.15\,\lambda_0$), that is, it maximizes the FOM at 4.6 dB. The performance of the antenna with the new GNDP is tabulated in Table 3 and Table 4.

Compact Array Model

Two 3rd-iteration sinusoidal monopoles (i = 3) were placed on a common PCB carrier, thus, their feed lines share the same GNDP and the same substrate. The model is shown in perspective in Figure 7. The distance of the feed points from the sides of the PCB is 9 mm, or half the optimum GNDP width. The interelement distance is a design variable. The feed lines are excited by ports placed on equivalent square SMA connectors. As shown in Figure 8, when the distance of the elements is $0.15\,\lambda_0$, there is strong coupling between the two antennas. In the following sections we quantify the severity of this coupling.

Parametric Study and Numerical Results

We varied the interelement distance from $0.25\,\lambda_0$ (= 30 mm) down to $0.10\,\lambda_0$ (= 12 mm). Figure 9 depicts the vari-

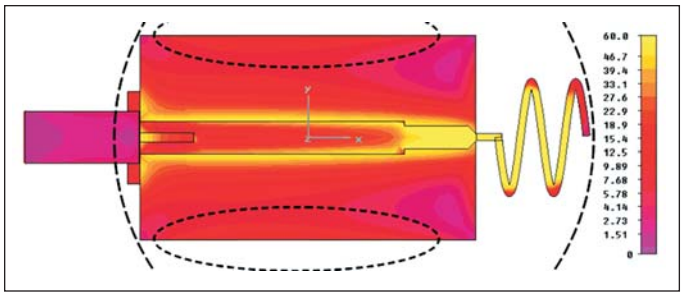

Figure 6 · The surface current distribution of the 4th iteration sinusoidal antenna at the frequency of the first resonance (near 2.5 GHz). The image depicts concurrent maximum values, which is physically unrealizable because of phase shifting. The ellipses indicate the winged nature of the surface current. The dashed circle represents the size of the radiansphere. Only conductive parts of the PCB are shown.

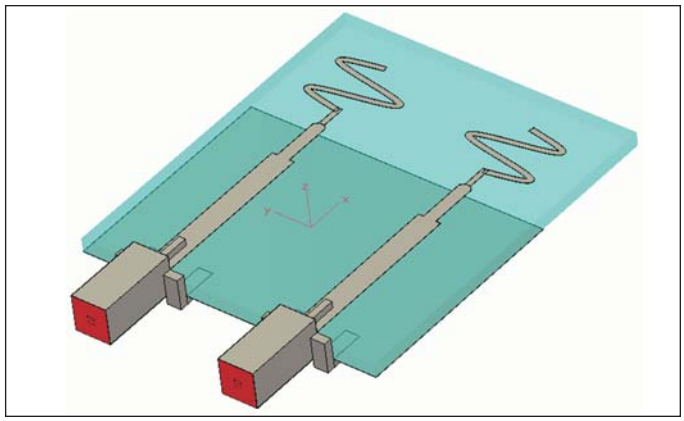

Figure 7 · A perspective view of the 2-element compact array. The FR4 substrate is transparent so that the GNDP is visible. In this snapshot the interelement distance is 18 mm (0.15 λ_0).

ation of input matching. By comparison to the results of Figure 3, it is obvious that the upper adjacent resonance has vanished, while the first resonances shifted lower. These are due to the presence of the other element and to the much wider GND plane, which does not benefit sinusoidal antennas. However, large bandwidths are observed in the 2-3 GHz range; ranging from 0.5 GHz to 0.7 GHz, with respective fractional bandwidths of 20% to 28%. The resonances lie in the range $2.32 < f_{res} < 2.48$ GHz, whereas the centers lie in the range $2.39 < f_c < 2.51$ GHz.

Moreover, the results in Figure 10 show the variation of mutual coupling in terms of the scattering parameter $S_{21}(j\omega)$. The worst-case coupling reaches $S_{21max} = -4.5$ dB for the smallest interelement distance. Such strong coupling would probably render this multi-element antenna useless for MIMO systems. Only at $\lambda_0/4$ spacing is the coupling reduced to –10 dB. In order to test for MIMO compliance, we calculated the envelope coefficient of the array from the complex scattering parameters [13, 14].

$$\rho_e = \frac{\left|S_{11}^* S_{12} + S_{21}^* S_{22}\right|^2}{\left(1-\left(|S_{11}|^2+|S_{21}|^2\right)\right)\left(1-\left(|S_{21}|^2+|S_{22}|^2\right)\right)} \quad (4)$$

Using S parameters instead of far-field data for this estimation assumes that the angles-of-arrival at the vicinity of the receiver are uniformly spread [14]. In our case, the approximation is good because large angular spreads occur in sensor networks (e.g., indoor deployments). In the event of a reciprocal and symmetrical array, (4) can be simplified as in (5):

$$\rho_e' = \frac{\left|2\,\mathrm{Re}\left\{S_{11}S_{21}^*\right\}^2\right|}{\left(1-|S_{11}|^2-|S_{21}|^2\right)^2} \quad (5)$$

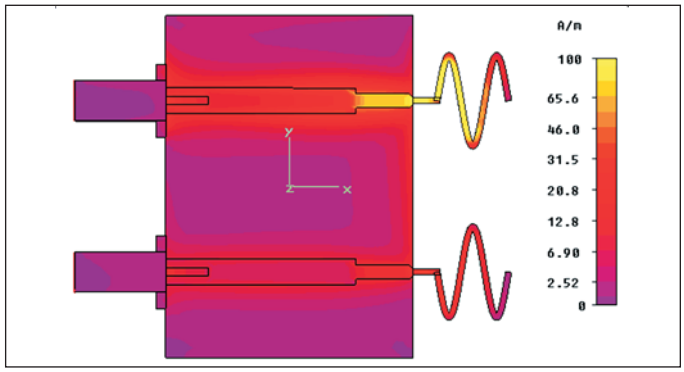

Figure 8 · Port 1 is excited (top), while Port 2 is terminated with 50 Ω (bottom). The surface current distribution on the conductive parts demonstrates one of the main mechanisms of mutual coupling.

Contrary to all expectations, the results in Figure 11 show great promise: The correlation coefficient is estimated lower than 0.35 even for a spacing $d_{min} = 12$ mm = $0.10\ \lambda_0$.

A Simple Technique That Reduces Mutual Coupling and Envelope Correlation

There exist certain scenarios where it would be desirable or even mandatory to reduce coupling between the elements of the array. For example, the estimation of ρ_e via the S parameters might prove to be optimistic, due to low antenna efficiency. Although not mentioned in the original work [13], the expression derived by the authors is based on the power balance of impinging, coupled and radiated fields; therefore, it assumes total radiation efficiency equal to unity. The designer might even wish to bring the feed points of the elements even closer than $\lambda_0/10$. Since the modeled elements share a common

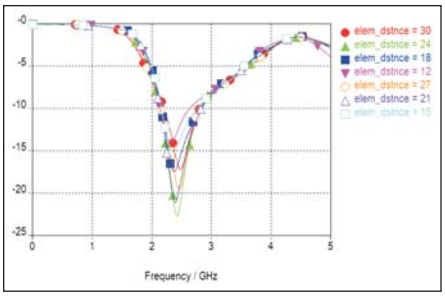

Figure 9 · Parametric study of the broadband input matching for different values of interelement distance (0.25 λ_0 to 0.10 λ_0).

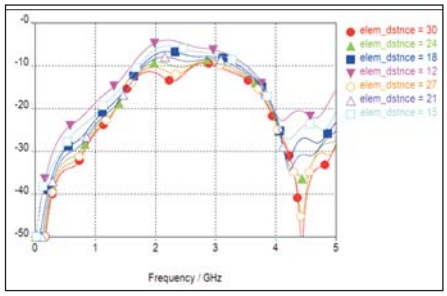

Figure 10 · Parametric study of the broadband mutual coupling for different values of interelement distance (0.25 λ_0 to 0.10 λ_0).

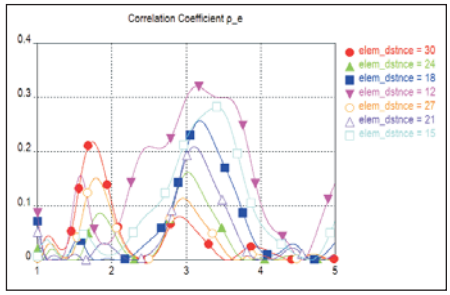

Figure 11 · Parametric study of the broadband envelope correlation for different values of interelement distance (0.25 λ_0 to 0.10 λ_0).

GNDP, a simple way to achieve this is to use a defected ground structure (DGS); see Figure 12.

Defected Ground Structures

Defected ground planes are an evolution of photonic bandgap (PBG) structures from the optical regime towards microwave frequencies [15]. Contrary to PBG structures, they are usually non-periodic [16]. The DGS unit cell can be modeled near the resonance frequency as a parallel RLC circuit in series and between two segments of transmission line. Park [17] suggested a slightly more complex equivalent circuit by adding shunt resistances and capacitances at the two reference planes of the defect. That work also included a way to extract the values of the circuit elements from the ABCD-parameters of the two-port defect. The ABCD-parameters can be extracted from the S parameters of the structure, which are obtained after simulation in E/M solvers or measurement of actual hardware. Karmakar et al. provided a quasi-static analysis of the most frequently occurred defect, i.e., the dumbbell DGS [18]. Their analysis attempts to quantify the contribution from every part of the defect in the frequency response.

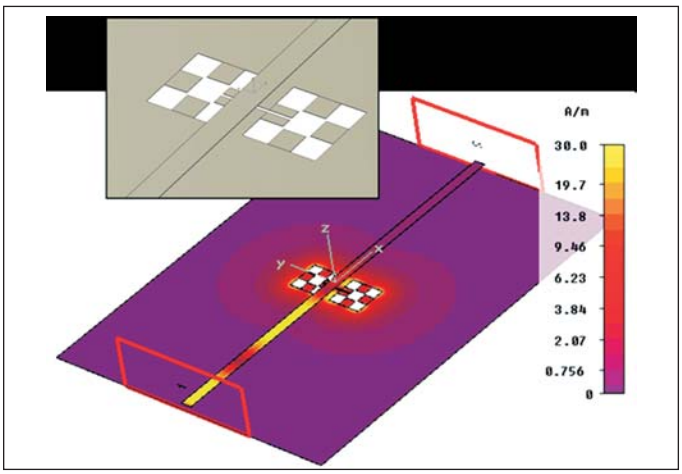

Figure 12 · The proposed pre-fractal defected ground structure. The current distribution is calculated at the resonance frequency, where the DGS acts as an open circuit and creates a standing wave pattern on the line.

DGSs have been studied extensively for the past decade, and they have been successfully applied in the design of filters and amplifiers. Their versatility has also found use in the antenna field [19], though not nearly as much as in microstrip filters and amplifiers. The properties of the DGS as a resonator are given by (6) and (7),

$$Q = \frac{R}{\omega_0 L} = \omega_0 RC \tag{6}$$

$$FBW_{3\,\mathrm{dB}} = \frac{1}{Q} \tag{7}$$

where ω_0 is the resonance frequency, Q is the quality factor, $FBW_{3\mathrm{dB}}$ is the 3-dB fractional bandwidth of the stopband, and $R/L/C$ denote total distributed resistance, inductance and capacitance at resonance.

The proposed DGS is shown in the model of Figure 12, where the defect has been etched below a microstrip line (the substrate was made invisible). It is based on the dumbbell DGS, but it was eventually given a pre-fractal shape, a first-order Sierpinski carpet. Its overall dimensions are 19 × 8 mm. The electrical performance of the DGS is shown in Figure 13, where a wide stopband is formed around 2.5 GHz. In terms of signal transmission, the defect acts mainly as an open-circuit, which creates a standing-wave pattern across the line. It also acts partially as an antenna. The resonance is not very deep; this is a low-Q structure, estimated from the 3-dB fractional BW at Q = 1.3. Nevertheless, this is just a blessing in disguise: The 30-dB rejection is more than enough for the reduction of mutual coupling, while the low Q-factor of the resonator makes the stopband wide enough to match the BW of the antenna.

DGS-Loaded Compact Array Antenna

The concept behind the proposed technique is to insert

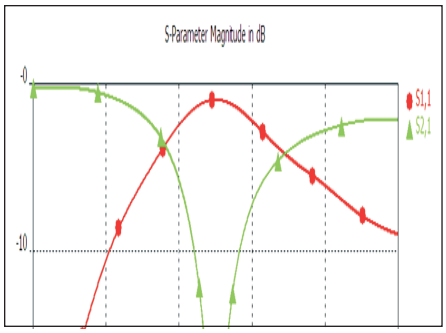

Figure 13 · The proposed DGS resonates at 2.5 GHz, causing high reflection and little signal transmission around that frequency.

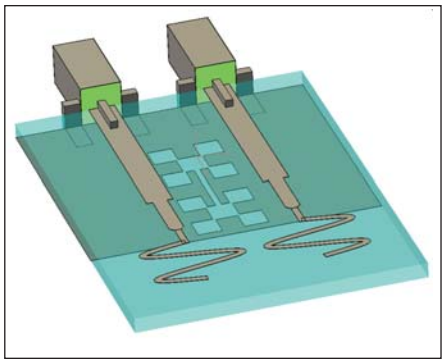

Figure 14 · Perspective view of the 2-element compact array with embedded DGS.

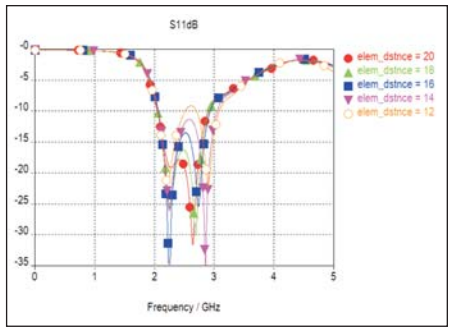

Figure 15 · Parametric study of the broadband input matching of the DGS-loaded array for interelement distances of 0.17 λ_0 to 0.10 λ_0.

the DGS between the two elements of the array and estimate the reduction in mutual coupling. As shown in Figure 14, the pre-fractal DGS is inserted (etched away) perpendicular to the flow of current between the two elements. This is an attempt to block the ground currents that contaminate the signal of the other antenna (the "signal bleed"). The PCB area occupied by the DGS decoupler is 17.3 × 7.3 mm, or $0.14\ \lambda_0 \times 0.06\ \lambda_0$.

The frequency response of the defected array in Figure 15 shows that the disturbance of the current caused by the DGS still leads to a working antenna with a 1-GHz operational BW. Clearly, the interelement distance affects the input impedance; this can be handled by re-sizing the elements and re-matching at the feed point. The current disturbance and the resonant behavior of the DGS offer a multi-decibel drop in mutual coupling measured in terms of $S_{21}(j\omega)$. For the 0.17 λ_0 distance the drop is 10 dB, while for the 0.10 λ_0 distance we gain more than 15 dB of reduction in coupling.

This reduction was also studied in terms of envelope correlation coefficient, which is an established metric for multi-element antennas. The results in Figure 17 depict the broadband envelope correlation caused by the DGS when the two elements are spaced $\lambda_0/10$ apart. The DGS that was applied is shown in Figure 18. The width of the long slot (nominally set at 0.6 mm) is one of the crucial

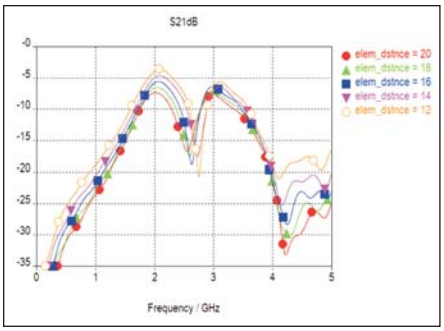

Figure 16 · Parametric study of the broadband mutual coupling of the DGS-loaded array for interelement distances of 0.17 λ_0 to 0.10 λ_0.

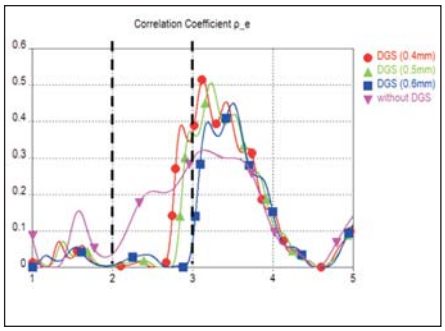

Figure 17 · Significant reduction of the envelope correlation in the 2-3 GHz range was achieved with the DGS at λ_0/10.

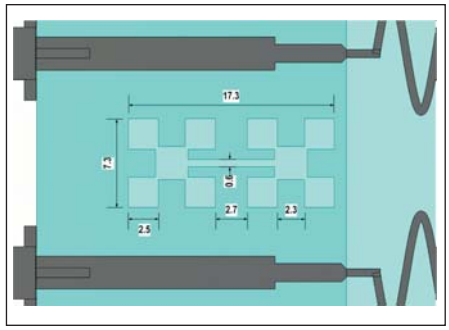

Figure 18 · A closer look at the proposed PBG structure on the GNDP (FR4 substrate made transparent). All dimensions are in mm.

dimensions of the defect, because it controls the distributed capacitance.

We used three different values for the slot width. This study shows that as the slot widens, the defect becomes more "wideband," i.e., its stopband widens. Eventually, when we used the 0.6-mm wide slot, the envelope correlation was practically eliminated inside the operating BW_V of the antenna element. In this way, the DGS bandgap is translated into a correlation bandgap for the array.

Conclusion and Future Work

The design process described in this paper has shown numerically the benefits of bending a printed monopole according to the sinusoidal curve. Sinusoidal monopoles show good potential for integration into portable devices. The second-iteration sinusoidal antenna built around a GNDP that measured 28 mm × 16 mm demonstrated peak performance among the six iterations. It achieved a bandwidth of 1.43 GHz (50%), while its frequency-averaged total efficiency was calculated above 80%. The electrical size of the overall radiator was ka = 1.26 rad.

Sinusoids function well with relatively small GND planes. They provide ease of building compact printed arrays. Some detuning takes place, although it is not severe and can be compensated. The frequency response showed graceful degradation with denser spacing. What is more, extreme values of mutual coupling did not lead to extreme envelope correlation.

Eventually CMOS integrated circuits will advance to the point of enabling diversity and MIMO applications on tiny sensor nodes. Antenna technology has to keep up with this trend. By inserting a simple defect in the GND plane, we managed to practically eliminate mutual coupling inside the band of interest and form a correlation bandgap. The proposed technique is cost-effective since it is compatible with PCB printing processes, and offers multi-decibel gains in coupling and correlation reduction.

Future work involves the experimental validation of the presented design process by measurements on actual prototypes; this procedure is already under way. More work is needed on the defect itself: It has to be made even smaller in terms of the wavelength to enable closer antenna packing. Dielectric loading with a material of higher dielectric constant must be avoided, because it would compromise antenna efficiency. It would also be very useful to discover ways to make its stopband even more wideband. Finally, we plan to extend this technique to four-element compact arrays, which are much more appealing to MIMO system applications, because they can extract the full rank of a realistic environment that is rich in scatterers.

References

1. I. F. Akyildiz, T. Melodia, and K. R. Chowdury, "Wireless multimedia sensor networks: A survey," *Wireless Commun.,* vol. 14, pp. 32-39, Dec. 2007.

2. A. R. Lopez, "Fundamental limitations of small antennas: Validation of Wheeler's Formulas," *IEEE Antennas Prop. Mag.,* vol. 48, no. 4, pp. 28-36, Aug. 2006.

3. A. K. Skrivervik, J.-F. Zuercher, O. Staub, and J. R. Mosig, "PCS antenna design: The challenge of miniaturization," *IEEE Antennas Prop. Mag.,* vol. 43, no. 4, pp. 12-27, Aug. 2001.

4. C. G. Kakoyiannis and P. Constantinou, "Co-design of Antenna Element and Ground Plane for Printed Monopoles Embedded in Wireless Sensors," in *Proc. Int'l Conf. on Sensor Technologies & Applications* (SENSORCOMM'08), Cap Esterel, pp. 413-418, Aug. 2008.

5. C. G. Kakoyiannis, G. Stamatiou, and P. Constantinou, "Small square meander-line antennas with reduced ground plane size for multimedia WSN nodes," in *Proc. Third European Conf. Antennas Prop.* (EuCAP 2009), pp. 2411-2415, Berlin, March 2009.

6. C. G. Kakoyiannis, P. Gika, and P. Constantinou, "Small Printed Sinusoidal Antennas: A Simple Design Guide for Smooth Meander-line Structures with

Augmented Bandwidth," *Int'l Workshop on Antenna Technology: Small Antennas and Novel Metamaterials* (iWAT2009), to be published.

7. M. Ali and S. S. Stuchly, "Short sinusoidal antennas for wireless communications," in *Proc. IEEE Pacific Rim Conf. Commun. Computers Signal Processing,* pp. 542-545, May 1995.

8. M. Ali, S. S. Stuchly, and K. Caputa, "An experimental study of small self-resonant antennas for wireless applications," *Microwave Opt. Technol. Lett.,* vol. 35, no. 2, pp. 143-145, 2002.

9. C. G. Kakoyiannis, P. Gika, and P. Constantinou, "Compact Multi-Element Antennas of Sinusoidal Printed Monopoles for Sensors and Portable Devices," in *Proc. Third European Conference on Antennas and Propagation,* (EuCAP'09), pp. 3423-3427, Berlin, March 2009.

10. S. G. García, L. Baggen, D. Manteuffel, and D. Heberling, "Study of coplanar waveguide-fed antennas using the FDTD method," *Microwave Opt. Technol. Lett.,* vol. 19, pp. 173-176, 1998.

11. CST Microwave Studio, *User Manual Version 2006,* Sep. 2005, CST GmbH, www.cst.com.

12. M. Martinez-Vazquez, R. Serrano, J. Carlsson, and A. K. Skrivervik, "Activities on terminal antennas in ACE2," in *Proc. Int'l Conf. Applied Electromagn. & Commun.* (ICECom'07), Dubrovnik, pp. 81-84, 2007.

13. S. Blanch, J. Romeu, and I. Corbella, "Exact representation of antenna system diversity performance from input parameter description," *Electronics Letters,* vol. 39, no. 9, pp. 705-707, May 2003.

14. J. Thaysen and K. B. Jakobsen, "Design considerations for low antenna correlation and mutual coupling reduction in multi antenna terminals," *Euro. Trans. Telecomms.,* vol. 18, pp. 319-326, 2007.

15. C.-S. Kim, J.-S. Park, D. Ahn, and J.-B. Lim, "A novel 1-D periodic defected ground structure for planar circuits," *IEEE Microw. Guided Wave Lett.,* vol. 10, no. 4, pp. 131-133, April 2000.

16. D. Ahn et al., "A design of the low-pass filter using the novel microstrip defected ground structure," *IEEE Trans. Microw. Theory Tech.,* vol. 49, no. 1, pp. 86-93, Jan. 2001.

17. J.-S. Park, "An equivalent circuit and modeling method for defected ground structure and its application to the design of microwave circuits," *Microwave Journal,* vol. 46, no. 11, pp. 22-44, Nov. 2003.

18. N. C. Karmakar, S. M. Roy, and I. Balbin, "Quasi-static modeling of defected ground structure," *IEEE Trans. Microw. Theory Tech.,* vol. 54, no. 5, pp. 2160-2168, May 2006.

19. Y. Chung et al., "Multifunctional microstrip transmission lines integrated with defected ground structure for RF front-end application," *IEEE Trans. Microw. Theory Tech.,* vol. 52, pp. 1425-1432, May 2004.

Author Information

Constantine Kakoyiannis received the Diploma in Electrical and Computer Engineering from the National Technical University of Athens (NTUA), Greece, in 2000. He has been a research associate with the Mobile Radio Communications Laboratory of the NTUA since 2001, where he is currently pursuing a Doctor of Engineering degree. Interested readers may contact him by e-mail at: kkak@mobile.ntua.gr

Penelope Gika studied Electrical and Computer Engineering at the National Technical University of Athens, Greece and received the Engineering Diploma in 2008. Her diploma thesis was on small printed multiband antennas shaped after analytical curves. She is currently pursuing a Master of Science degree in Communications Engineering at RWTH Aachen University.

Philip Constantinou received the Master of Applied Science in Electrical Engineering from the University of Ottawa, Canada, in 1976, and the Ph.D. degree in Electrical Engineering from Carleton University in 1983. In 1989 he joined the National Technical University of Athens where he is a Professor and Director of the Mobile Radio Communications Laboratory. His current research interests include personal communications, mobile satcom, interference problems, and radiation hazard.